Normal vector analysis from GNSS–GPS data applied to Deception volcano surface deformation

M. Berrocoso,[1] G. Prates,[1,2] A. Fernández-Ros[1] and A. García[3]

[1]*Laboratorio de Astronomía, Geodesia y Cartografía, Departamento de Matemáticas, Facultad de Ciencias, Campus Río San Pedro, Universidad de Cádiz, 11510 Puerto Real (Cádiz), Spain. E-mail: manuel.berrocoso@uca.es*
[2]*Departamento de Engenharia Civil, Instituto Superior de Engenharia, Universidade do Algarve, Faro, Portugal*
[3]*Departamento de Volcanología, Museo Nacional de Ciencias Naturales, Consejo Superior de Investigaciones Científicas, Madrid, Spain*

GJI Mineral physics, rheology, heat flow and volcanology

SUMMARY

Surface deformation parameters and its use in volcano monitoring have evolved from classical geodetic procedures up to those based on Global Navigation Satellite Systems (GNSS), in particular the most widely used and known Global Positioning System (GPS), profiting from the automated data processing, positioning precision and rates, as well as the large storage capacity and low power consumption of its equipments. These features have enabled the permanent GNSS–GPS data acquisition to ensure the continuous monitoring of geodetic benchmarks for the evaluation of surface deformation in active tectonic or volcanic areas. In Deception Island (Antarctica), a normal vector analysis is being used to give surface deformation based on three permanently observed GNSS–GPS benchmarks. Due to data availability, both in the past and for near real-time use, all benchmarks used are inside the monitored volcanic area, although the reference is away from thermal springs and/or fumaroles, unlike the other two. The time variation of slope distances to the reference benchmark and of the magnitude and inclination of the normal vector to the triangle defined by the reference benchmark and any other two, provides the spatial deformation in the volcanic area covered. The normal vector variation in magnitude gives information on compression or expansion, here called spatial dilatometer, while the changes in inclination gives information on relative uplift or subsidence, here called spatial inclinometer. In geodesy, the triangle is a basic geometric unit and the areal strain is commonly applied in tectonics and volcanism. The normal vector analysis conjugates both, benefiting from the method's precision, simplicity and possibility to model the surface using several triangles. The proposed method was applied to GNSS–GPS data collected every austral summer between 2001–2002 and 2009–2010 in Deception Island. The results evidence that Deception Island acts as a strain marker in the Bransfield Basin volcano-tectonic setting.

Key words: Satellite geodesy; Volcano monitoring; Antarctica.

1 INTRODUCTION

Deception Island is a horseshoe-shaped stratovolcano, situated in the Bransfield Strait extensional basin between the South Shetland Islands to the west and the Antarctic Peninsula to the east, whose main volcano-tectonic feature is a central flooded depression. This central caldera has been traditionally described as a collapse caldera originated after one or more voluminous eruptions (Smellie 2001). However, other models suggest that its formation was due to a progressive passive normal faulting along a nearly orthogonal fault system that cuts across the Island according to a regional trend (Rey *et al.* 1995; Marti *et al.* 1996). The region defined by the South Shetland Archipelago, the Bransfield Sea and the Antarctic Peninsula is dynamically complex due to its tectonic surroundings. Two major plates converge, the South American and the Antarctic

plates and several minor plates interact, the Scotia, the Phoenix and the South Shetland plates (Fig. 1) (Galindo-Zaldívar *et al.* 2004; Maestro *et al.* 2007).

The South Shetland Archipelago is a volcanic arc formed as a consequence of the Phoenix microplate subduction under the Antarctic Plate, whose rate is near 1.0 cm yr^{-1} (Dietrich *et al.* 2001; Robertson-Maurice *et al.* 2003; Taylor *et al.* 2008; Jin *et al.* 2009). The slow subduction rate is favourable to the roll back motion of the subducted slab, producing the extension of the overriding plate and giving way to the back arc Bransfield Basin formation, and thus to the separation of the South Shetland Block. To the north, the South Shetland Trench ends at the left-lateral Shackleton Fracture Zone near Elephant Island and to the south, ends at the Hero Fracture Zone, whose southeastward direction goes by Deception Island. Furthermore, due to the Antarctic Plate northeastward
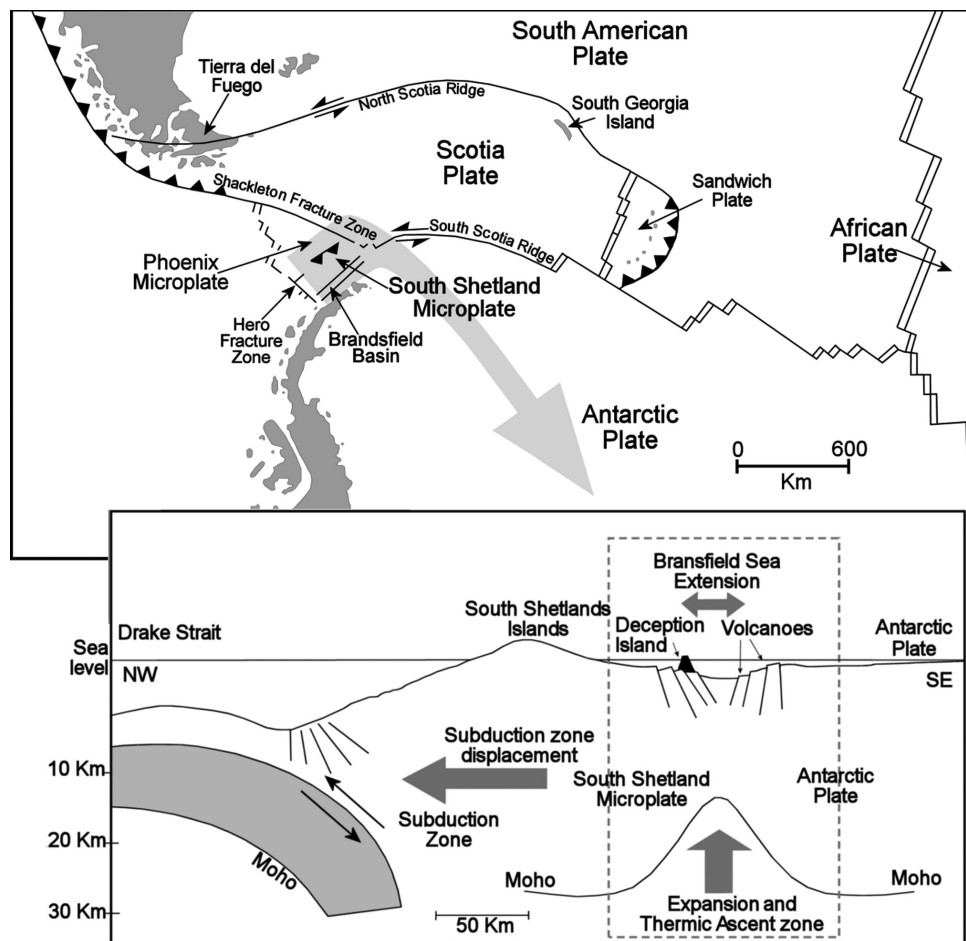
Figure 1. Tectonic setting showing the Scotia, the Phoenix and the South Shetland plates, bounded by the major Antarctic and South American plates.

movement in this region, the South Shetland Trench has an additional left-lateral component that extends to the left-lateral transpressive South Scotia Ridge, the Antarctic–Scotia Plate boundary, which may compete with the slab roll back as the main mechanism for the Bransfield Basin extensional regime (Galindo-Zaldívar *et al.* 2004; Maestro *et al.* 2007). These mechanisms are the cause of the nearly orthogonal fault system, following the NNW–SSE and NNE–SSW directions, that is present in the Bransfield Basin (Maestro *et al.* 2007).

The central area of the Bransfield Basin is the most active, between Bridgeman Island and Deception Island, with near 60 km width, 230 km long and 1950 m deep. It has asymmetrical edges, more abrupt on the South Shetland Islands side, with maximum slope of 25°–30° and about 10 km long and smoother on the Antarctic Peninsula side (González-Ferrán 1991; Canals *et al.* 1997; Galindo-Zaldívar *et al.* 2004). The active volcanism in this area is characterized by emergent volcanoes like Deception, Penguin and Bridgman, and also by numerous submarine volcanoes with different evolution stages, from well defined volcanic cones to its obliteration as a consequence of the existing extensional tectonic regime (Canals *et al.* 1997). These volcanic centres are aligned following the NNE–SSW basin main direction. The volcanic activity is manifested by historical eruptions in Deception and Penguin Islands, together with rifting and magmatic processes during the last 2 Myr. These facts suggest that the volcanic activity in the Bransfield Basin goes on in continuous development (González-Ferrán 1991).

Deception Island has undergone a nearly continuous volcanic activity, with confirmed eruptions in 1800, 1812, 1842, 1871, 1912, 1956, 1967 and 1970. The last eruptive process from 1967 to 1970 was located around Telephone Bay and Mount Pond, along a main fracture in the NNE–SSW direction. It gave rise to a 40-m-high cone and an alignment of five craters in the northern sector of the Island, causing the collapse of the Chilean Base in Pendulum Cove and the destruction of the British Base in Whalers Bay due to a lahar action. This situation forced every scientific task developed in the island to be suspended (González-Ferrán & Katsui 1970; González-Ferrán 1995) until the first Spanish–Argentinean campaigns restored the Island's volcano monitoring. Nowadays, the main superficial evidences of volcanic activity in the Island are the presence of fumarolic areas with 100 °C and 70 °C gaseous emissions at Fumarole and Whalers Bay respectively; 100 °C hot soil in Cerro Caliente; and 45 °C and 65 °C thermal springs in Pendulum Cove and Whalers Bay, respectively (Garcia *et al.* 1997; Ibáñez *et al.* 2000). A remarkable seismic activity is also registered in the Island. The high seismicity reflects the basin extension, the subduction process and the volcanism. Most of these events are shallow, with low energy content and magnitudes between 1 and 2. Volcano-tectonic (VT) earthquakes of magnitude 3 and 4 were also detected during the seismovolcanic crisis in 1991–1992 and 1998–1999 (Ibáñez *et al.* 2000, 2003). The seismovolcanic crisis in 1992 January had a noticeable activity increase with 900 events registered and four felt earthquakes. Detected gravity and magnetic anomalies suggested

that the volcanic reactivation was due to a 2000-m-depth magmatic injection near Fumarole Bay (Ibáñez *et al.* 2000). These evidences started to diminish in 1992 February. Repeated GNSS–GPS surveying from 1989–1990 to 1995–1996 registered on Fumarole Bay and Whalers Bay the most significant ground deformations (Berrocoso 1997). Also, near the end of 1998, the few seismic events recorded suddenly changed at the beginning of 1999, when a significant seismovolcanic activity was detected. This crisis included VT and long-period events together with volcanic tremors. Most of the registered events were located between Fumarole and Telephone Bay, some of which were large enough to be felt, with magnitude 3 and 4. When the campaign finished, towards the end of February, the seismic activity was still high (Ibáñez *et al.* 2003). A series of geophysical measurements were registered, from which it was concluded that the volcano's reactivation occurred, reflected in the deformation rate increase, in the gas composition change and in the gravity and magnetic anomalies. These evidences suggested an injection of fresh magma to a depth of 500–1000 m, where the most affected area was Fumarole Bay (García *et al.* 2002; Berrocoso *et al.* 2006). Recent geomagnetic, gravimetric and seismic refraction studies further support the existence of a magma chamber underneath Deception's flooded caldera (Somoza *et al.* 2004; Muñoz-Martín *et al.* 2005; Zandomeneghi *et al.* 2009). Seismic refraction and tomography profiles suggest that Port Foster is underlain by a magma chamber that extends downward from 2000 m to at least 5000 m depth. The stronger low velocity anomalies detected beneath Fumarole Bay are consistent with the presence of a significant volume of partial melt (Zandomeneghi *et al.* 2009), although smaller low velocity anomalies were indentified as well under Mount Pond.

2 GEODETIC INFRASTRUCTURE

Geodetic studies in Deception Island began in the 1950's by the Chilean, Argentinean and British scientists from bases established on the Island. These works were mainly directed to update the existing cartography of the Island and were interrupted at the end of the 1960's, when the last eruptive process forced the bases evacuation. The geodetic and geophysical studies were suspended until 1987, when the volcano monitoring was re-established by Spanish and Argentinean researchers, that since have been running geomagnetic, gravimetric and seismic refraction measurements, as well as geochemical and geodetic studies. The tectonic behaviour of the Antarctic Peninsula, concerning to the South America and the South Shetland Archipelago, has been the motivation of some projects from Scientific Committee Antarctic Researches (SCAR), with episodic campaigns developed to survey the increasing number of GNSS–GPS benchmarks distributed along this region (Dietrich *et al.* 2001). Throughout the several Spanish Antarctic campaigns the REGID geodetic reference frame was constructed (Fig. 2a). This reference frame was designed with the aim of enabling geodynamic studies based on GNSS–GPS geodetic techniques (Berrocoso *et al.* 2008). It is formed by 15 benchmarks on Deception Island's inner ring, from which that located near the Spanish Base Gabriel de Castilla BEGC is considered the reference benchmark, benefiting from the Base's logistic. A reference benchmark is needed for the sub-centimetre precision expected when differential GNSS–GPS positioning is used to achieve geodynamic capability. Furthermore, to ensure the correct and well-known position of the GNSS–GPS antenna centre relatively to the benchmark at each campaign, a forcing system was designed, based on a 5-cm-

stainless steel screw for the benchmark materialization and a laboratory measured prolongation with nearly 13 cm to attach the antenna (Fig. 2b).

Until now the GNSS–GPS data collected at the REGID benchmarks was used to establish successive volcano surface deformation models, nevertheless without continuous and near real-time capability. The models were based on episodic observation periods, for the majority of the benchmarks not more than 5–6 d each austral summer campaign. Although the REGID reference frame grants spatial homogeneity, the same does not occur with the time of the ground deformation. Since 2001, added to the reference benchmark BEGC, FUMA benchmark at Fumarole Bay and PEND benchmark at Pendulum Cove became permanently observed along all campaign extent. This two benchmarks are located near the main fracture where the 1967–1970 eruptive process occurred, additionally having superficial evidences of volcanic activity, like fumaroles or thermal springs. Also, both seismovolcanic crisis of 1992 and 1999 were caused by magma injection near Fumarole Bay (Ibáñez *et al.* 2000; García *et al.* 2002). From the 2007–2008 campaign, a wireless connection infrastructure is being developed so that the data collected in the three sites can be processed at near real time on a monitoring station.

From the continuous satellite observation at the benchmarks BEGC, FUMA and PEND, relative ground deformation monitoring at Fumarole Bay and Pendulum Cove near real time can be achieved, while BEGC is considered fix. To establish the ground deformation history at these sites, the data collected each austral summer since 2001–2002 until 2009–2010 were processed to attain positioning solutions every 30 min. The GNSS–GPS receivers and antennas used were geodetic, measuring in both L1 and L2 frequencies. The registered sampling rate in the first two campaigns was 30 s, then until 2004–2005 was 15 s and in the last campaigns, a 1 s rate was used.

3 METHODS

The Bernese GPS Software 5.0 (Dach *et al.* 2007) was used to process the GNSS–GPS data to attain positioning solutions every 30 min. However, a 3 h previous solution was computed to determine the cycle ambiguities with the quasi-ionosphere-free technique (Mervart 1995), where ionospheric total electron content grids were used, and one tropospheric zenith delay correction per hour, using both the hydrostatic model and the mapping functions by Niell (1996). The average percentage of ambiguities solved with this strategy was near 85 per cent. Then, 30 min solutions were processed using the double-differenced ionosphere-free combination, a $10°$ cut-off angle and precise ephemerides, along with the pre-processed ambiguity solutions and the tropospheric zenith delay corrections. The ocean loading effect was considered as well. All other systematic errors were treated according to the Center for Orbit Determination in Europe processing standards for the International GNSS Service (IGS), provided with the Bernese Processing Engine (Dach *et al.* 2007). For near real-time solutions, the processing strategy needs minor adjustments due to the unavailability of ionospheric total electron content grids and precise ephemerides, consequently decreasing the precision level. However, the solutions can be reprocessed using the IGS rapid products (Dow *et al.* 2009) with an approximated 24 h delay.

Nevertheless, the enabled positioning precision and its 30 min rate makes possible to detect half-day periodicities, certainly of non-volcanic origin, that need to be filtered. The origin of these
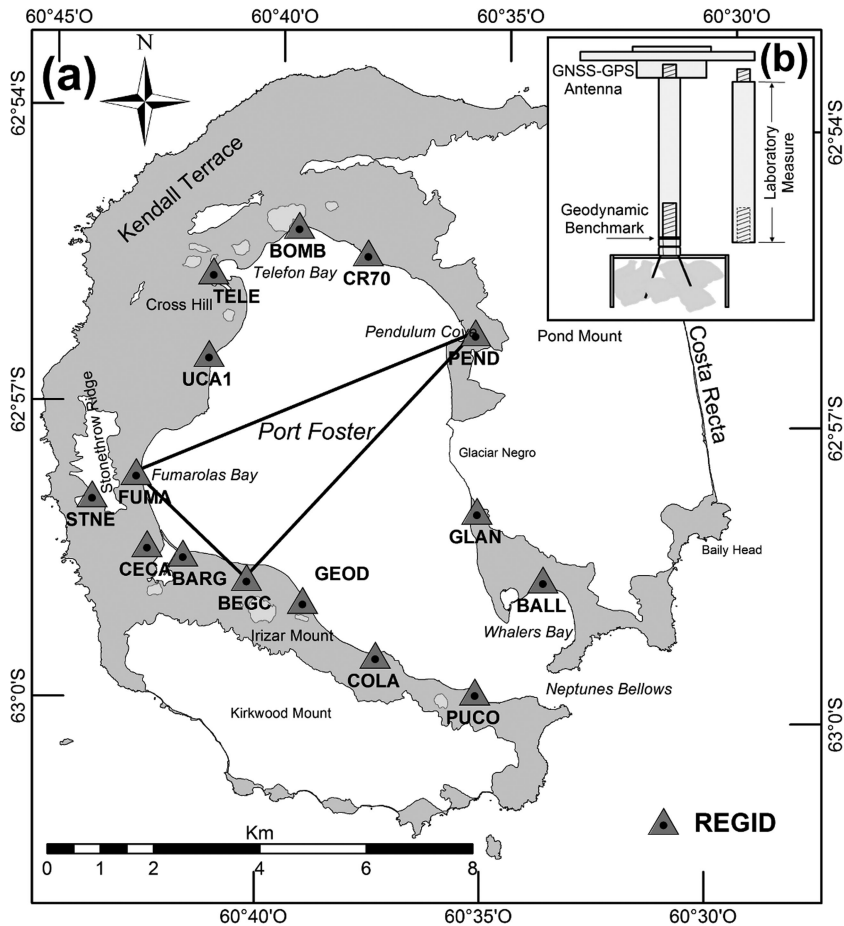
Figure 2. The REGID (Red Geodésica Isla Decepción) spatial distribution (a) and antenna position forcing system (b).

half-day periodicities is yet to be thoroughly studied, but residual effects not corrected by the models used for the ocean tide loading or driven by the near 12 h constellation orbital period may be suggested. Due to the Gaussian distribution of these residual periodic effects, a Discrete Kalman Filter (Kalman 1960) was designed and implemented. Its prediction model was based on the average increment registered in the last 12 h filtered solutions, the stability component, slightly corrected with the tendency attained for the 30 min prior to the predicted solution, the reactive component,

$$
\hat{x}_k = x_{k-1} + w_{\mathrm{R}} \frac{x_{k-1} - x_{k-2}}{t_{k-1} - t_{k-2}} \left(t_k - t_{k-1}\right)
$$
$$
+ w_{\mathrm{S}} \frac{x_{k-1} - x_{k-25}}{t_{k-1} - t_{k-25}} \left(t_k - t_{k-1}\right),
$$

where w_{S} and w_{R} are the stability and reactive components weights respectively, x represent the filtered solutions, $\hat{x}$ the predicted solution and t the solution's time.

The Discrete Kalman Filter is a recursive state-space method that, given a good prediction model and with observations affected by Gaussian white noise, should maintain the same average whatever the considered time interval used in both observed and filtered time-series, after removing the phase-shift that typically affects recursive filters. The filtered solution is given by correcting the model predicted solution with a fraction, known as Kalman gain K, of the difference between the predicted solution and the observed solution z, at step k, that when both represent the same parameter is written

as

$$
x_k = \hat{x}_k + K_k \left(z_k - \hat{x}_k\right).
$$

The Kalman gain tends to neglect the standard difference between the predicted and the observed solutions, which should be similar to the observations standard noise R_k. Then the filtered solutions noise P_k tends to the product of the observations standard noise with the Kalman gain. This is a consequence of the Kalman gain expression that, when predicted and observed solutions represent the same parameter and the filtered solutions noise is much smaller than the observations standard noise ($P_k \ll R_k$), can be simplified to

$$
K_k \approx \frac{P_{k-1}}{R_k}, \; P_{k-1} \ll R_k.
$$

The implemented Discrete Kalman Filter gave an overall Kalman gain of 0.1, considering all campaigns and observed (Bernese processed) time-series, resulting in a 90 per cent noise reduction in each time-series.

For continuous volcano-tectonic monitoring, the time variation of each benchmark topocentric coordinates can provide information about the deformation of the ground where it is linked. Through the time variation of the baseline's slope distance relative to the reference benchmark lineal deformation can be identified. The time variation of the three benchmarks position, where one can be the reference benchmark, gives the time variation of the triangle defined by them, which normal vector provides information about its

spatial deformation. In particular conditions the triangle's spatial deformation can be related to the volcano's spatial deformation, needing the same general volcano-tectonic source to be the cause of each local ground deformation, which is not straightforward. Furthermore, in differential GNSS–GPS the reference benchmark is held fix, and when its movement is unknown and though unremoved, only the baseline's northing, easting and height components can be measured. The advantage of slope distance and normal vector analysis is that the reference's movement is part of both baseline's and triangle's variation. BEGC, FUMA and PEND benchmarks are the vertices of the triangle subjected to normal vector analysis, in particular its normal vector's magnitude and inclination. As the normal vector's magnitude of two adjacent sides of a parallelogram is numerically equal to the parallelogram's area and being the triangle's area half the parallelogram's, the variation of the normal vector's magnitude is an indicator of compression or extension of the triangle due to the simultaneous ground deformation at the three sites, here called spatial dilatometer. Moreover, the variation of the normal vector's inclination is an indicator of ground deformation as well, showing relative uplift or subsidence between the three sites, here called spatial inclinometer. The normal vector was computed by the external product of the vectors defined by the BECG–FUMA
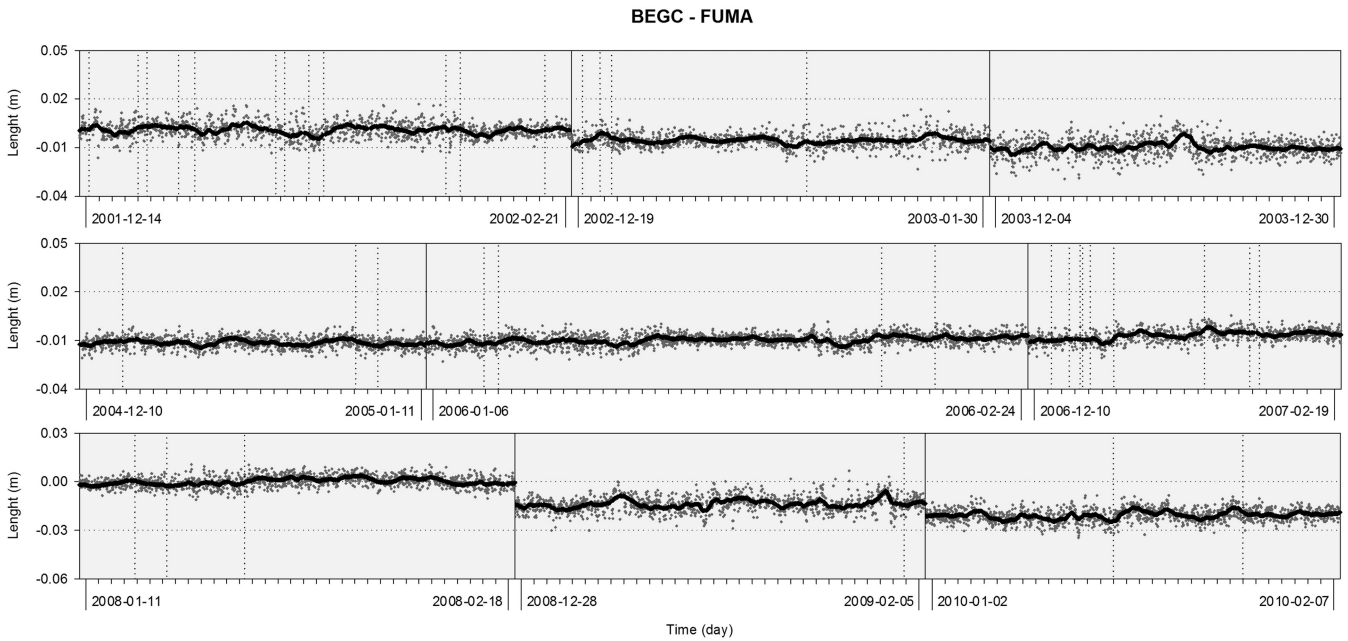

Figure 3. BEGC–FUMA slope distance time-series. Bernese solutions (grey) and filtered solutions (black). Full vertical lines between campaigns. Doted vertical lines when data gaps occur.
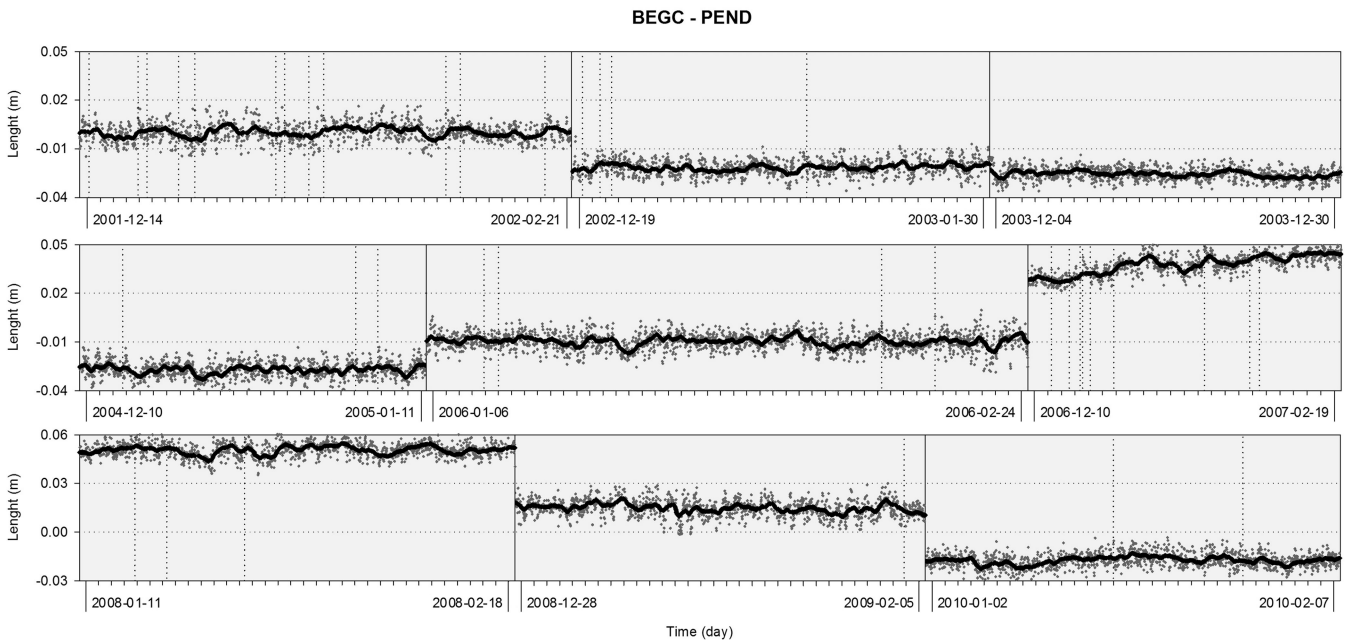

Figure 4. BEGC–PEND slope distance time-series. Bernese solutions (grey) and filtered solutions (black). Full vertical lines between campaigns. Doted vertical lines when data gaps occur.

segment and the BEGC–PEND segment, respectively u and v, at each time

$$\vec{n} = \vec{u} \times \vec{v} = (dn_{BF}, de_{BF}, dh_{BF}) \times (dn_{BP}, de_{BP}, dh_{BP}),$$

where dn_{BF}, de_{BF} and dh_{BF} are the BECG–FUMA baseline's northing, easting and height components and dn_{BP}, dn_{BP} and dn_{BP} are the BECG–PEND baseline's northing, easting and height components.

4 RESULTS AND ANALYSIS

The time-series of Bernese processed solutions have an overall average root mean square (rms) of 1 cm in the northing and easting components and of 2 cm in the height component, with Gaussian distribution. Nevertheless, due to the characteristic small deformations at Fumarole Bay and Pendulum Cove during these campaigns, a clearer understanding of the ground deformation is accomplished analysing the filtered time-series, profiting from the 0.1 Kalman gain and expected average rms reduction of 90 per cent as discussed previously, resulting in a precision of 0.1 cm in the northing and easting components and of 0.2 cm in the height component. In Figs 3 and 4, the baselines slope distance time-series are presented, furthermore showing the implemented Discrete Kalman Filter efficiency.

Although a geodetic benchmark is available in Livingston Island 36 km from Deception, data availability in the studied campaigns
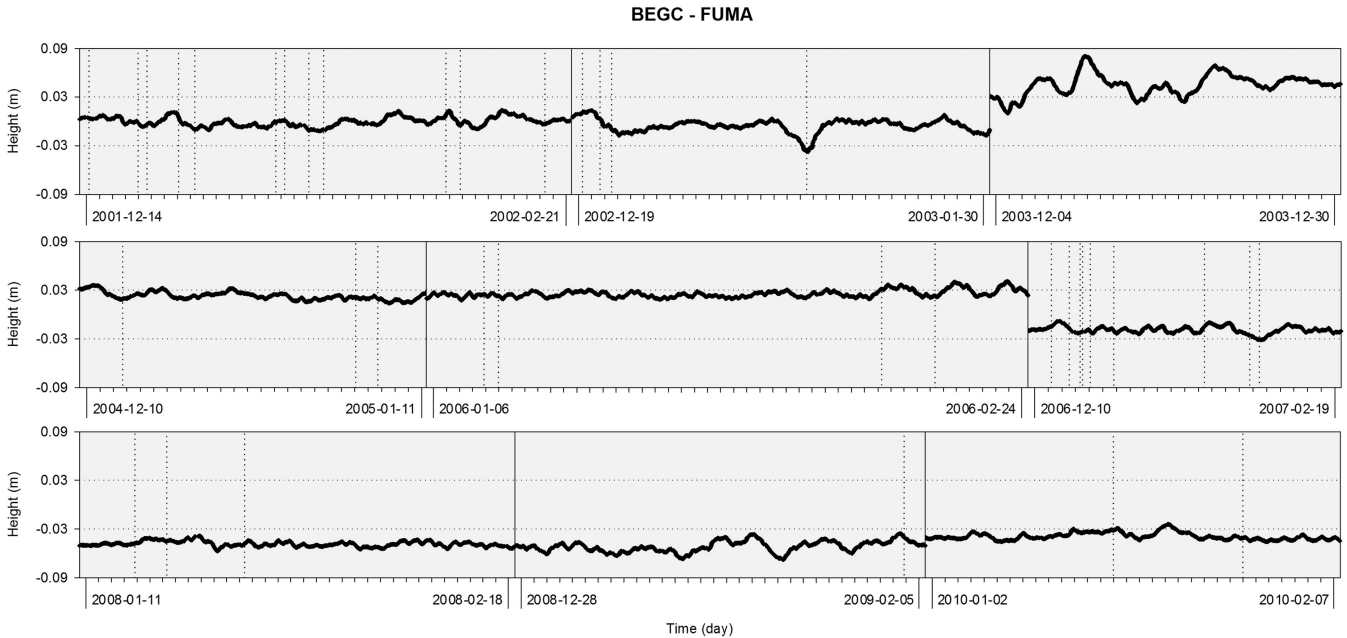

Figure 5. BEGC–FUMA baseline's height component filtered solutions time-series.
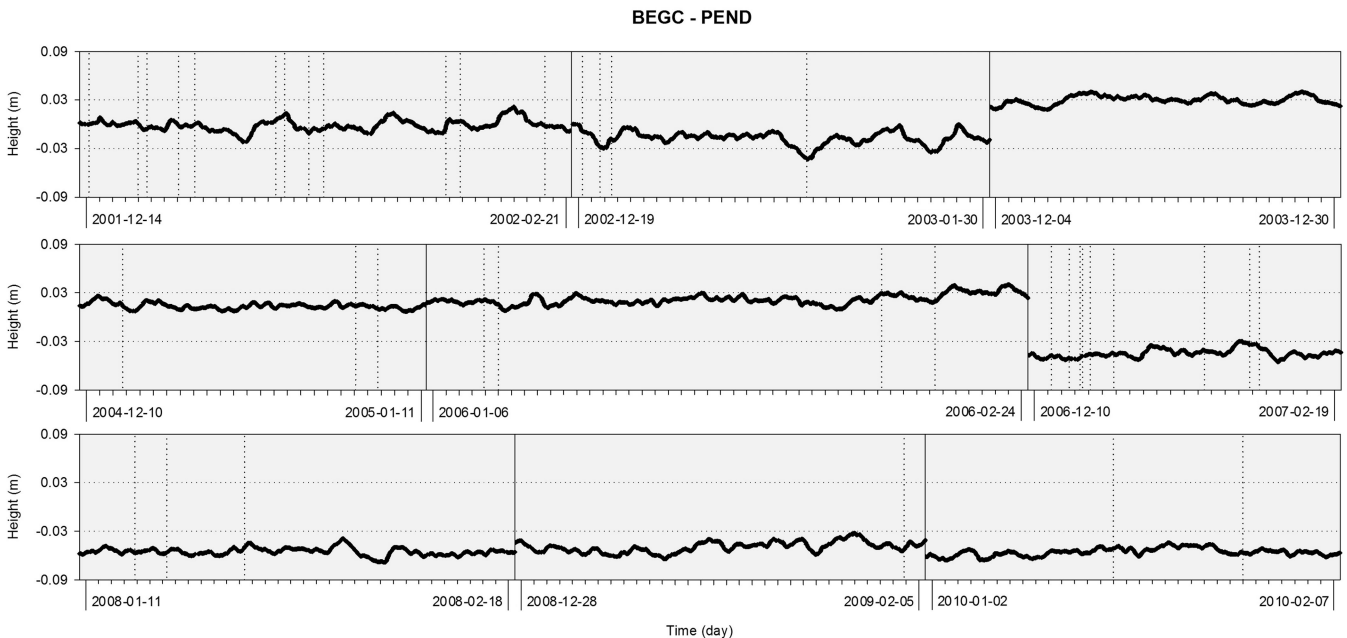

Figure 6. BEGC–PEND baseline's height component filtered solutions time-series.

is lesser and for present near real-time use is still inaccessible. For that reason, BEGC was chosen as the reference benchmark, allowing for unremoved ground deformation there, especially for baseline's slope distance and triangle's normal vector analysis. Still, because the baseline's slope distance is almost unaffected by its height component variation, unlike by its northing and easting components and its information shouldn't be neglected, the baselines height component time-series are presented in Figs 5 and 6. Comparing BEGC–FUMA and BEGC–PEND baselines height component time-series little correlation is detected. Moreover based on the benchmarks location, the measured variations are better explained by ground deformation at Fumarole Bay and Pendulum Cove. During the 2003–2004 campaign, the larger deformation events are

shown in FUMA's time-series, where a relative to BEGC uplift of near 8 cm in 3 d was measured followed by a relative subsidence of near 6 cm in 2 d.

The time-series for the spatial dilatometer and the spatial inclinometer are presented, respectively in Figs 7 and 8. The spatial dilatometer time-series shows when and how the changes from compressive (decreasing magnitude) to extensive (increasing magnitude) occur in the triangle based on the three benchmarks, from where the areal strain rates (Sigmundsson *et al.* 1995; Ferhat *et al.* 1998) can be further computed. During the 2006–2007 campaign, a triangle's 23 ppm yr^{-1} extension rate was registered, between December 9 and February 20. Also, between campaigns, a compressive state was identified from 2002 until 2004 followed by an
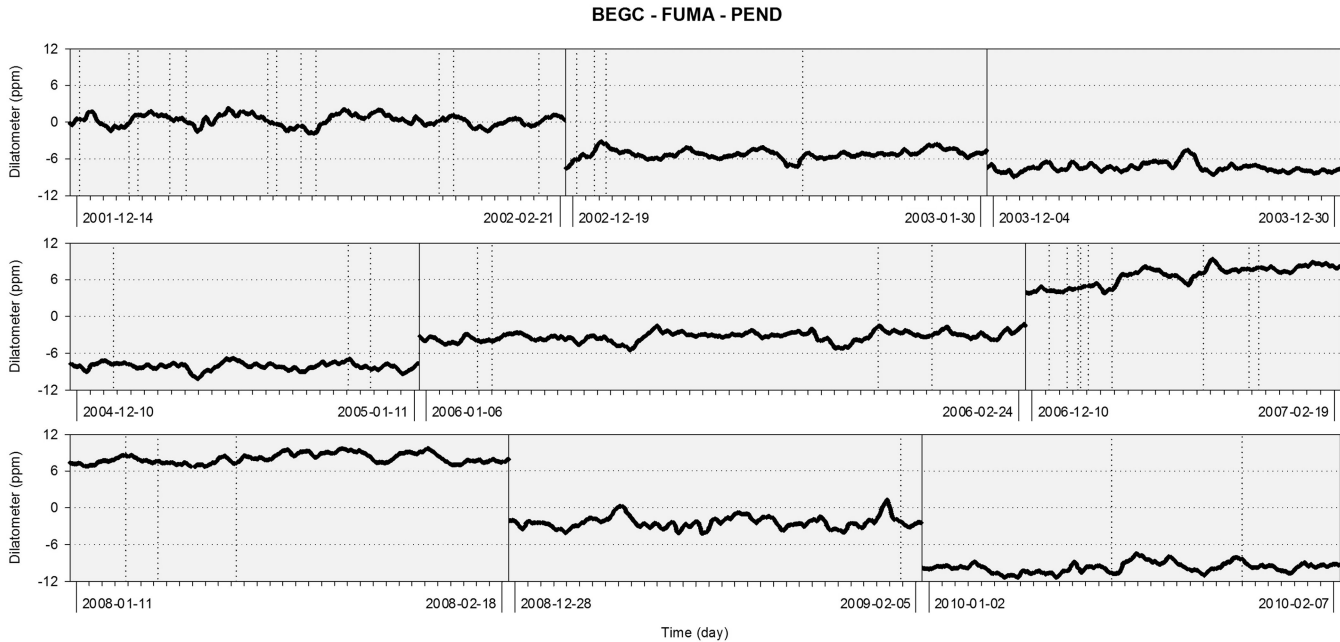

Figure 7. BEGC, FUMA and PEND benchmarks based triangle spatial dilatometer time-series.
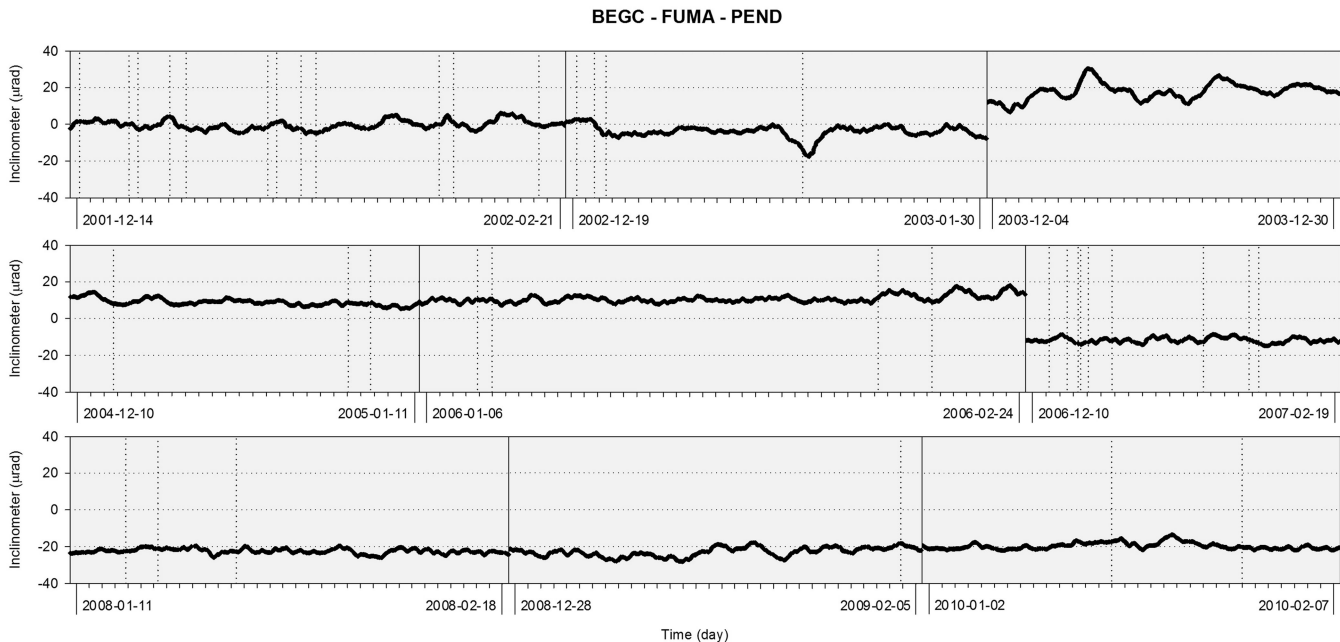

Figure 8. BEGC, FUMA and PEND benchmarks based triangle spatial inclinometer time-series.

extensive state from 2005 until 2007 and then by another compressive state from 2008 until 2010.

The spatial inclinometer time-series increases as the triangle tends to define a horizontal plan, meaning that the height difference between benchmarks becomes lesser, whereas a decrease in inclination indicates the opposite. Although ambiguity exists about the benchmarks vertical deformation without each baseline's height component time-series, only the spatial inclinometer needs to be observed to follow the changes in the triangle's inclination. Among campaigns a significant spatial inclinometer decrease was identified during the year of 2006, since the 2005–2006 campaign ended in 2006 February and the 2006–2007 campaign begun in 2006 December, related with FUMA and PEND getting respectively, near 5 cm and 7 cm lower, with respect to BEGC.

5 CONCLUSIONS

Deception Island is a volcanic island in a high tectonic stress setting. There, the ground deformation can be due to volcanic activity, but has well caused by slab rollback and slab subduction at the South Shetland Trench or by the left-lateral transpressional stress along the South Scotia Ridge. When slab rollback is the foremost regime, extension of the Bransfield Basin is expected and due to normal faulting some subsidence is probable. If either slab subdution at the South Shetland Trench or left-lateral transpressional stress along the South Scotia Ridge are the main regime, compression of the Bransfield Basin should be expected and caused by thrust faulting some uplift may occur. During inflation of a magma chamber, compression and subsidence at the volcano surface may occur due to isostactic adjustment or extension and uplift due to pressure increase (Dzurisin 2007). Furthermore, the benchmarks location with respect to a possible magma chamber is critical. Due to Deception's location in the Bransfield Basin, the complex volcanic interpretation of ground deformation has an additional tectonic component, resulting that the Island acts as a strain marker for the volcano-tectonic setting. Nevertheless, these two parameters may be interesting enough to help separate from volcanic or tectonic as the foremost regime present, together with other geophysical data, if the spatial inclinometer can provide unambiguous information about uplift and subsidence as the spatial dilatometer can about extension and compression. Still, the separation among short-term events and long-term between campaigns signal should be accounted for, as episodic events are better explained by volcanic activity and long-term signal by tectonic stress regimes.

The implemented Kalman Filter gave valid solutions for the most probable deformation, free from the effect of the half-day periodicities encountered in the GNSS–GPS processing solutions, possibly caused by some residual uncorrected tidal or driven by the orbital period effects. Although small, several deformation events can be identified that, if thought of volcanic origin, evidence a highly active volcano considering the fact that it is monitored only 2–3 months in a year.

The spatial dilatometer registered a triangle's 23 ppm year^{-1} extension rate during the 2006–2007 campaign. Along the studied campaigns a 3 yr period of compression was followed by another 3 yr period of extension and then again by a 3 yr period of compression. The spatial inclinometer identified the relative to BEGC vertical deformation of either FUMA and/or PEND evidenced by its correlation with BEGC–FUMA baseline's height component in the 2003–2004 and with BEGC–PEND baseline's height component in 2007–2008. A significant spatial inclinometer decrease was

identified during the year of 2006. The proposed method's precision and simplicity enables its use in near real-time conditions providing information about surface deformation even if all geodetic benchmarks are inside the volcanic area, based on two parameters: extension through the spatial dilatometer and inclination thru the spatial inclinometer.

REFERENCES

Berrocoso, M., 1997. *Modelos y Formalismos para el Tratamiento de Observaciones GPS. Aplicación al Establecimiento de Redes Geodésicas y Geodinámicas en la Antártida,* Boletín ROA No. 1/97, Real Instituto y Observatorio de la Armada, San Fernando.

Berrocoso, M., Ramírez, M.E. & Fernández-Ros, A., 2006. Horizontal deformation models for the Deception Island, in *Geodetic Deformation Monitoring: From Geophysical to Engineering Roles,* Vol. 131, pp. 217–221, eds Sansó, F. & Gil, A.J., International Association of Geodesy Symposia (IAG), Springer-Verlag, Berlín.

Berrocoso, M. *et al*., 2008. Geodetic research on Deception Island and its environment (South Shetland Islands, Bransfield Sea and Antarctic Peninsula) during Spanish Antarctic Campaigns (1987–2007), in *Geodetic and Geophysical Observations in Antarctica,* pp. 97–124, eds Capra, A. & Dietrich, R., Springer-Verlag, Berlin.

Canals M., Gracia, E. & Grupo GEBRA, 1997. Evidence of initial seafloor spreading in the Central Bransfield Basin, Western Antarctica, *Boletín Real Sociedad Española de Historia Natural (Sección Geología),* **93**(1–4), 53–61.

Dach, R., Hugentobler, U., Fridez, P. & Meindl, M. (eds), 2007. Bernese GPS Software Ver. 5.0 User manual, 612 p., Astronomical Institute, University of Bern.

Dow, J.M., Neilan, R.E. & Rizos, C., 2009. The International GNSS Service in a changing landscape of Global Navigation Satellite Systems, *J. Geod.,* **83**(7), 191–198.

Dietrich, R. *et al*., 2001. ITRF coordinates and plate velocities from repeated GPS campaigns in Antarctica – an analysis based on different individual solutions, *J. Geodyn.,* **74,** 756–766.

Dzurisin, D., 2007. *Volcano Deformation: New Geodetic Monitoring Techniques,* 441 pp., Springer-Verlag, New York.

Ferhat, G., Feigl, K.L., Ritz J.F. & Souriau, A., 1998. Geodetic measurement of tectonic deformation in the southern Alps and Provence, France, 1947–1994, *Earth planet. Sci. Lett.,* **159,** 35–46.

Galindo-Zaldívar, J., Gamboa, L., Maldonado, A., Nakao, S. & Bochu, Y., 2004. Tectonic development of the Bransfield Basin and its prolongation

to the South Scotia Ridge, northern Antarctic Peninsula, *Mar. Geol.,* **206**(1–4), 267–282.

Garcia, A., Blanco, I., Torta, J.M., Astiz, M.M., Ibáñez, J.M. & Ortiz, R., 1997. A search for the volcanomagnetic signal at Deception volcano (South Shetland I., Antarctica), *Annali di Geofisica,* **40**(2), 319–327.

García, A. & DECVOL Working Group, 2002. A crossdisciplinary study at Deception Island (South shetland Islands, Antarctica). Evaluation of the recent volcanological status, Consejo Superior de Investigaciones Científicas, Museo Nacional de Ciencias Naturales, Madrid.

González-Ferrán, O. & Katsui, Y., 1970. *Estudio integral del volcanismo cenozoico superior de las Islas Shetland del Sur, Antartica, Serie Científica,* Vol. 1, pp. 123–174, Instituto Antartico Chileno, Punta Arenas, Chile.

González-Ferrán, O., 1991. The Bransfield rift and its active volcanism, in *Geological Evolution of Antarctica,* pp. 505–509, eds Thomson, R.A., Crame, J.A. & Thomson, J.W., Cambridge University Press, Cambridge.

González-Ferrán, O., 1995. *Volcanes de Chile,* lnstituto Geográfico Militar, Santiago de Chile, Chile.

Ibáñez, J.M., del Pezzo, E., Almendros, J., la Rocca, M., Alguacil, G., Ortiz, R. & García, A., 2000. Seismovolcanic signals at Deception Island Volcano, Antarctica: wavefield analysis and source modelling, *J. geophys. Res.,* **105**, 13 905–13 931.

Ibáñez, J.M., Carmona, E., Almendros, J., Saccorotti, G., del Pezzo, E., Abril, M. & Ortiz, R., 2003. The 1998–1999 seismic series at Deception Island volcano, Antarctica, *J. Volc. Geotherm. Res.,* **128**(1–3), 65–88.

Jin, Y.K., Lee, J., Hong, J.K. & Nam, S.H., 2009. Is subduction ongoing in the South Shetland Trench, Antarctic Peninsula?: new constraints from crustal structures of outer trench wall, *Geosci. J.,* **13**(1), 59–67.

Kalman, R.E., 1960. A New Approach to Linear Filtering and Prediction Problems, *J. Basic Eng.,* **D-82**, 35–45.

Maestro, A., Somoza, L., Rey, J., Martinez-Frias, J. & Lopez-Martinez, J., 2007. Active tectonics, fault patterns, and stress field of Deception Island: a response to oblique convergence between the Pacific and Antarctic plates, *J. South Am. earth sci.,* **23**, 256–268.

Marti, J., Vila, J. & Rey, J., 1996. Deception Island (Bransfield strait, Antarctica): an example of collapse caldera developed by extensional tectonics, in *Volcano Instability on the Earth and other Planets,* pp. 253–265, eds McGuire, W.C., Jones, A.P. & Neuberg, J., Geological Society Special Publication, London, UK.

Muñoz-Martín, A., Catalán, M., Martín-Dávila, J. & Carbó, A., 2005. Upper crustal structure of Deception Island area (Bransfield Strait, Antarctica) from gravity and magnetic modelling, *Antarct. Sci.,* **17**, 213–224.

Mervart, L., 1995. Ambiguity resolution techniques in geodetic and geodynamic applications of the global positioning system, *PhD thesis.* University of Bern.

Niell, A.E., 1996. Global mapping functions for the atmosphere delay at radio wavelengths, *J. geophys. Res.,* **101**(B2), 3227–3246.

Rey, J., Somoza, L. & Martínez-Frías, J., 1995. Tectonic, volcanic, and hydrothermal event sequence on Deception Island (Antarctica), *Geo-Mar. Lett.,* **15**(1), 1–8.

Robertson-Maurice, S.D., Wiens, D.A., Shore, P.J., Vera, E. & Dorman, L.M.M., 2003. Seismicity and tectonics of the South Shetland Islands and Bransfield Strait from a regional broadband seismograph deployment, *J. geophys. Res.,* **108**(B10), 2461–2472.

Sigmundsson, F., Tryggvason, E., Alves, M.M., Alves, J.L., Pálsson, K. & Ólafsson, H., 1995. Slow inflation of the Furnas Volcano, São Miguel, Azores, suggested from initial leveling and global positioning system measurements, *Geophys. Res. Lett.,* **22**(13), 1681–1684.

Smellie, J.L., 2001. Lithostratigraphy and volcanic evolution of Deception Island, South Shetland Islands, *Antarct. Sci.,* **13**, 188–209.

Somoza, L., Martínez-Frías, J., Smellie, J.L., Rey, J. & Maestro, A., 2004. Evidence for hydrothermal venting and sediment volcanism discharged after recent short-lived volcanic eruptions at Deception Island, Bransfield Strait, Antarctica, *Mar. Geol.,* **203**(1–2), 119–140.

Taylor, F.W. *et al.*, 2008. Kinematics and segmentation of the South Shetland Islands-Bransfield basin system, northern Antarctic Peninsula, *Geochem. Geophys. Geosys.,* **9**(Q04035), doi:10.1029/2007GC001873.

Zandomeneghi, D., Barclay, A., Almendros, J., Ibañez Godoy, J.M., Wilcock, W.S.D. & Ben-Zvi, T., 2009. Crustal structure of Deception Island volcano from P wave seismic tomography: tectonic and volcanic implications, *J. geophys. Res.,* **114**(B06310), doi:10.1029/2008JB006119.